STABILITY OF GEOTACTIC BIOCONVECTION: ANALYTICAL BOUNDS AND NUMERICAL THRESHOLDS *

JIABAO NIE †, MARTINA BUKAČ†, AND CATALIN TRENCHEA ‡

Abstract. This work is focused on the stability analysis of the bioconvection model, which describes spontaneous flow patterns arising in suspensions of motile microorganisms. The instability is driven by biased swimming and the resulting density stratification. Parameter regimes that delineate the onset of bioconvection are investigated. The instability mechanism is analogous to Rayleigh-Bénard convection but originates from microbially generated density variations rather than temperature gradients. We conduct linear stability analysis, where a nonhomogeneous vertical drift term appears. This term couples the separable modes in Rayleigh's formulation, making the derivation of explicit analytical stability criteria impossible. **(a)** To address this difficulty, we introduce an approximation method that yields theoretically rigorous upper and lower bounds for the onset of instability. The critical stability condition is further estimated using several tractable approximations. **(b)** To complement the analysis, we perform fully resolved time-dependent simulations of the governing equations. Using a bisection strategy, we compute numerical stability thresholds and assess the sharpness of the analytical predictions. Both approaches are applicable to general layer depths and can be readily extended to more complex drift or transport models. The results provide both promising analytical bounds and practical predictive tools for systems in which bioconvective mixing plays a significant role and for their various applications.

Relevance to Life Sciences. Bioconvection arises when motile microorganisms collectively generate fluid motion, affecting nutrient transport and mixing in natural and engineered environments. It is commonly observed in algal cultures, microbial bioreactors, and wastewater treatment systems. Whether such flow patterns develop depends on factors such as the strength of upward swimming, cell concentration, and fluid depth. Our results identify the parameter regimes in which bioconvective patterns emerge, providing quantitative thresholds that distinguish when mixing will occur and when suspensions will remain uniform. These predictions support the design and control of engineered microbial culture systems.

Mathematical Content. The bioconvection process is modeled by a coupled system of partial differential equations that describes microorganism transport and fluid motion. Starting from the steady state solution, the linear stability analysis is performed in order to determine the onset of flow patterns. We also carry out computational experiments using the finite element method. By systematically varying parameters and employing a bisection search, we identify the critical thresholds numerically and compare them to our theoretical results.

Key words. Bioconvection, Linear Stability, Numerical Thresholds, Rayleigh Number

MSC codes. 76E06, 92C17, 76R05, 65P40

1. Introduction.

The term *bioconvection* was first introduced by Platt in 1961 [32] to describe the macroscopic convective patterns that arise in dense suspensions of free-swimming microorganisms. This phenomenon, illustrated in Figure 1.1, has been observed across a broad spectrum of organisms, including algae, bacteria, and protozoa (e.g., [36, 35, 25]). In such suspensions, the collective upward swimming of motile microorganisms—typically slightly denser than the surrounding fluid—leads to their accumulation near the surface. This creates a denser top layer that becomes gravitationally unstable, ultimately giving rise to characteristic convection patterns reminiscent of Rayleigh-Bénard thermal convection [9].

Beyond its intrinsic scientific interest, bioconvection holds considerable promise for diverse industrial and environmental applications. These include microbial enhanced oil recovery, large-scale biofuel production [5, 6, 21], wastewater treatment

*Submitted to the editors DATE.

†Department of Applied and Computational Mathematics and Statistics, University of Notre Dame, Notre Dame, IN (jnie2@nd.edu, mbukac@nd.edu).

‡Department of Mathematics, University of Pittsburg, PA (trenchea@pitt.edu)

[28], and the design of microfluidic lab-on-a-chip systems [37]. Such applications underscore the broader significance of understanding the mechanisms that govern bioconvective flows and of identifying the conditions under which suspensions remain well mixed or become unstable.

Although bioconvection shares important features with Rayleigh-Bénard thermal convection-both featuring adverse density gradients that drive buoyancy-induced instabilities-the underlying physical origins differ. In thermal convection, density variations arise from temperature gradients, whereas in bioconvection they result from the active swimming and aggregation of microorganisms. This motility itself is governed by several taxis mechanisms, including oxytaxis (movement toward oxygen) [38], chemotaxis (movement toward nutrient) [40], and geotaxis (upward movement under the influences of gravity) [20], etc. Geotaxis, being exhibited by many algal species such as *Chlamydomonas nivalis*, has received particular attention and it has been widely studied as a dominant mechanism driving bioconvective instability.

The modeling of geotactic bioconvection has progressed through a series of increasingly sophisticated frameworks. Plesset and Winet [33] first likened the onset of bioconvection to a Rayleigh–Taylor instability by treating the organism-rich upper layer as a denser fluid overlying a lighter one. However, their formulation did not explicitly account for the negative geotaxis or swimming behavior of microorganisms. A more mechanistic framework was developed by Childress, Levandowsky and Spiegel (CLS) [11], who coupled the Navier-Stokes equations—augmented by a buoyancy term reflecting excess cell density—with an advection–diffusion equation for the cell concentration. Pedley, Hill, and Kessler [30] further extended this framework to describe the orientation distribution of swimming cells, providing a more detailed picture of gyrotactic effects, which refine geotaxis by incorporating orientation dynamics.

In parallel, a reduced form of the CLS model has been widely adopted, in which geotaxis is represented by an effective mean upward swimming velocity and isotropic diffusion is assumed (equal horizontal and vertical diffusivities) [16, 4]. This simplified CLS model, which we also employ in the present study, preserves the essential instability mechanism while remaining analytically and numerically tractable.

Alongside the development of mathematical models, substantial effort has been dedicated to the numerical simulation of bioconvective flows. Various computational approaches have been employed to solve the governing nonlinear system, including finite difference methods [16, 24, 1], spectral methods [12], and finite element formulations [14, 8]. These studies have been instrumental in reproducing characteristic plume patterns, exploring parameter dependencies, and validating continuum models against experimental observations. By capturing the fully nonlinear dynamics, numerical approaches complement analytical treatments and provide valuable insight into the rich behavior of bioconvective flows.

In parallel with numerical investigations, another important line of research has focused on elucidating the onset of instability in these systems. Early experiments established that characteristic patterns emerge only when the suspension depth or cell concentration exceeds certain thresholds [32]. Motivated by these observations, analytical investigations have sought to predict when uniform suspensions become unstable and develop organized flow structures. Drawing on the analogy with Rayleigh-Bénard convection, classical tools used for thermal convection, such as linear stability and asymptotic analyses, have been adapted to study bioconvective instabilities. Notably, Childress et al. [11], and Hill et al. [18] employed linear stability frameworks reminiscent of Rayleigh's original work on thermal convection [34]. Galdi and Straughan [15] investigated this problem by the method of nonlinear energy theory.

More recently, Avramenko et al. [2] applied a Lorenz-type approach [26] to analyze nonlinear transitions in bioconvective flow. Despite these advances, most existing studies rely on simplifying assumptions, such as shallow- or deep-layer limits, and comprehensive criteria valid across general parameter regimes remain scarce in the literature. Moreover, direct numerical verification of analytically predicted thresholds has been limited, leaving a gap between theory and fully resolved simulations.

In this work, we address these gaps by combining analytical and numerical approaches to develop a comprehensive stability theory for geotactic bioconvection. On the analytical side, we extend the classical linear stability framework by introducing a constant approximation for the non-uniform drift term, which yields explicit closed-form stability criteria and rigorous upper and lower bounds on the onset of instability. To complement the analysis, we carry out fully resolved time-dependent numerical simulations of the governing equations and employ a bisection strategy to accurately determine critical thresholds. This dual approach not only validates the theoretical predictions but also provides, for the first time, numerically computed stability conditions for the general bioconvection problem. By juxtaposing the analytical and numerical results, we offer a comprehensive characterization of the parameter regimes that lead to instability and quantify the influence of key parameters such as the Péclet number, excess cell density, and the upswimming velocity of the cells.

The remainder of this paper is organized as follows. In section 2, we present the mathematical model governing geotactic bioconvection and discuss the associated boundary conditions. Section 3 formulates the linear stability problem, including its non-dimensionalization and the resulting eigenvalue system. In section 4, we introduce the constant approximation method, deriving explicit stability criteria and bounds. Section 5 describes the numerical determination of stability thresholds using simulations and a bisection approach. Section 6 compares the analytical and numerical results, summarizes the main findings and, outlines directions for future work.

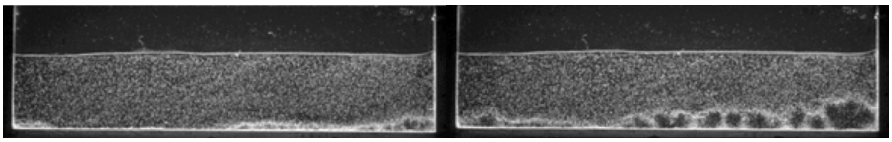

(a) $t = 3.0$ min (b) $t = 5.5$ min

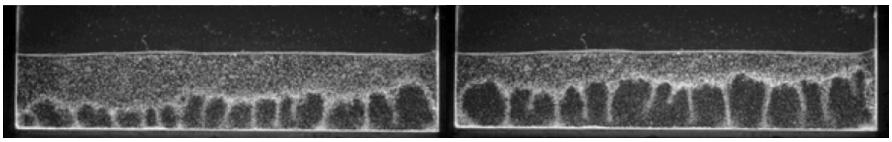

(c) $t = 8.0$ min (d) $t = 10.5$ min

FIG. 1.1. *Time sequence of bioconvective pattern development in a Hele–Shaw cell containing a suspension of Paramecium tetraurelia. Initially ($t = 0$) the suspension is uniform; the microorganisms swim upward against gravity, accumulating near the upper boundary. As the density increases, the top layer becomes gravitationally unstable, leading to descending plumes and the onset of bioconvection. Adapted from [23], reproduced with permission.*

2. Mathematical Model. The collective dynamics of negative geotactic microorganisms immersed in a viscous fluid can be modeled by the system of partial differential equations, coupling the Navier–Stokes equations with a convective transport

equation [11]:

$$\begin{aligned}
&\frac{\partial \mathbf{u}}{\partial t}(\mathbf{x},t) + (\mathbf{u}(\mathbf{x},t)\cdot\nabla)\mathbf{u}(\mathbf{x},t) - \frac{\mu}{\rho}\Delta\mathbf{u} = -\frac{1}{\rho}\nabla p(\mathbf{x},t) - (1+\mathbf{v}\gamma N(\mathbf{x},t))g\mathbf{i}_d,\\
&\nabla\cdot\mathbf{u}(\mathbf{x},t) = 0,\\
&\frac{\partial N}{\partial t}(\mathbf{x},t) - \Theta\Delta N(\mathbf{x},t) + (\mathbf{u}(\mathbf{x},t)\cdot\nabla)N(\mathbf{x},t) + W_c\nabla N(\mathbf{x},t)\cdot\mathbf{i}_d = 0.
\end{aligned} \tag{2.1}$$

Here $\mathbf{u}(\mathbf{x},t) = (u(\mathbf{x},t), v(\mathbf{x},t), w(\mathbf{x},t))$ and $p(\mathbf{x},t)$ denote the velocity and pressure of the culture fluid at position $\mathbf{x} = (x,y,z)$ and time $t > 0$, while $N(\mathbf{x},t)$ denotes the concentration of microorganisms. The vector $\mathbf{i}_d = (0,0,1)^T$ denotes the vertical unit vector. The parameters for the microorganisms and the culture fluid are given in Table 2.1.

TABLE 2.1
Parameters for the bioconvection model

Parameter	**Symbol**	**Units**
Height/Length of the domain	H/L	cm
Dynamic viscosity	μ	$\mathrm{g\,cm^{-1}\,s^{-1}}$
Density of culture fluid	ρ	$\mathrm{g\,cm^{-3}}$
Kinematic viscosity	$\nu = \mu/\rho$	$\mathrm{cm^2\,s^{-1}}$
Density of microorganisms	ρ_c	$\mathrm{g\,cm^{-3}}$
Microorganism density ratio	$\gamma = (\rho_c - \rho)/\rho$	–
Microorganism cell volume	$\mathbf{v}$	$\mathrm{cm^3}$
Gravitational acceleration	g	$\mathrm{cm\,s^{-2}}$
Diffusion rate of microorganisms	Θ	$\mathrm{cm^2\,s^{-1}}$
Upward swimming velocity	W_c	$\mathrm{cm\,s^{-1}}$
Average cell concentration	$\overline{N}$	$\mathrm{cm^{-3}}$

We assume that the fluid is bounded between two infinite parallel planes located at $z = 0$ and $z = H$. At these planes, the vertical velocity vanishes, while the microorganism concentration satisfies a no-flux condition:

$$\mathbf{u}\cdot\mathbf{i}_d = \mathbf{0}, \qquad \Theta\nabla N\cdot\mathbf{i}_d - W_c N = 0, \qquad z = 0, H. \tag{2.2}$$

Additional conditions are imposed on the vertical velocity component [11]. Assuming the boundary is free, the second derivative vanishes,

$$\frac{\partial^2}{\partial z^2}\big(\mathbf{u}\cdot\mathbf{i}_d\big) = 0, \qquad z = 0, H, \tag{2.3}$$

whereas assuming that the boundary is rigid, the first derivative vanishes,

$$\frac{\partial}{\partial z}\big(\mathbf{u}\cdot\mathbf{i}_d\big) = 0, \qquad z = 0, H. \tag{2.4}$$

In the horizontal directions, periodic boundary conditions are imposed to approximate an unbounded layer:

$$\mathbf{u}(0,y,z,t) = \mathbf{u}(L,y,z,t), \qquad N(0,y,z,t) = N(L,y,z,t). \tag{2.5}$$

This periodic setting serves as a computational surrogate for the idealized infinite horizontal extent.

The system admits a **steady equilibrium solution** when the velocity $\mathbf{u}$ vanishes [18],

$$\mathbf{u}_0 = \mathbf{0}. \tag{2.6}$$

We consider a steady-state concentration profile N_0 that is uniform in the horizontal directions (x, y), so that $N_0 = N_0(z)$ depends only on the vertical coordinate. This assumption is consistent with the physical context, as we are primarily interested in the onset of horizontal pattern formation from a vertically stratified equilibrium. Substituting into the governing equations (2.1), the steady-state concentration satisfies

$$\Theta \Delta N_0(z) - W_c \nabla N_0(z) \cdot \mathbf{i}_d = 0,$$

subject to the boundary conditions

$$\Theta \nabla N_0 \cdot \mathbf{i}_d - W_c N_0 = 0 \qquad \text{on } z = 0, H.$$

Solving this ordinary differential equation gives

$$N_0(z) = \overline{N}\, \frac{W_c H}{\Theta}\, \frac{1}{\exp\left(\frac{W_c H}{\Theta}\right) - 1} \exp\left(\tfrac{W_c}{\Theta} z\right). \tag{2.7}$$

Similarly, the steady pressure p_0, which also depends only on z, satisfies

$$\nabla p_0(\mathbf{x}, t) = -(\rho_c - \rho)\, \mathbf{v}\, N_0 g\, \mathbf{i}_d,$$

leading to the equilibrium pressure distribution

$$p_0(z) = -\,\overline{N} H (\rho_c - \rho) \mathbf{v} g \frac{1}{\exp\left(\frac{W_c H}{\Theta}\right) - 1} \exp\left(\tfrac{W_c}{\Theta} z\right). \tag{2.8}$$

3. Linear Stability Problem. In this section, we perform the linear stability analysis to identify the theoretical threshold for the onset of instability and pattern formation. As in Rayleigh-Bénard convection, the stability criterion not only predicts the loss of equilibrium, but also captures the emergence of patterns from a wide range of initial conditions.

3.1. Formulation of the Stability Problem. Let the initial steady state, described by equations (2.6), (2.7), and (2.8), be subject to small perturbations. The perturbed fields for velocity, pressure, and concentration are expressed as:

$$\begin{aligned} \mathbf{u}(\mathbf{x}, t) &= \mathbf{u}_0 + \epsilon\, \mathbf{u}_1(\mathbf{x}, t), \\ p(\mathbf{x}, t) &= p_0(z) + \epsilon\, p_1(\mathbf{x}, t), \\ N(\mathbf{x}, t) &= N_0(z) + \epsilon\, n(\mathbf{x}, t), \end{aligned} \tag{3.1}$$

where $0 < \epsilon \ll 1$ is the perturbation amplitude and $\mathbf{u}_1 = (u_1, v_1, w_1)$.

Substituting (3.1) into the governing equations (2.1) and retaining only $\mathcal{O}(\epsilon)$ terms yields

$$\begin{aligned} &\frac{\partial \mathbf{u}_1}{\partial t}(\mathbf{x}, t) \;-\; \frac{\mu}{\rho}\, \Delta \mathbf{u}_1 = -\,\frac{1}{\rho}\, \nabla p_1(\mathbf{x}, t) \;-\; \gamma\, \mathbf{v}\, n(\mathbf{x}, t)\, g\, \mathbf{i}_d, \\ &\nabla \cdot \mathbf{u}_1(\mathbf{x}, t) = 0, \\ &\frac{\partial n}{\partial t}(\mathbf{x}, t) \;-\; \Theta\, \Delta n(\mathbf{x}, t) \;+\; w_1\, \frac{dN_0}{dz} \;+\; W_c\, \nabla n(\mathbf{x}, t) \cdot \mathbf{i}_d = 0. \end{aligned} \tag{3.2}$$

To simplify notation, we omit the subscripts $_1$ in the remainder of the manuscript.

The pressure term p/ρ can be eliminated following the classical procedure described by Chandrasekhar [9, pp. 19–22] (see also [10, 13]) in the context of thermal convection. We introduce the vorticity vector

$$\boldsymbol{\eta} = \left(\frac{\partial w}{\partial y} - \frac{\partial v}{\partial z}, \frac{\partial u}{\partial z} - \frac{\partial w}{\partial x}, \frac{\partial v}{\partial x} - \frac{\partial u}{\partial y} \right), \tag{3.3}$$

and apply the curl operator to the momentum equation in (3.2). After a straightforward calculation, we reformulate the system as follows:

$$\frac{\partial \zeta}{\partial t} = \frac{\mu}{\rho} \nabla^2 \zeta, \tag{3.4a}$$

$$\frac{\partial}{\partial t} \nabla^2 w = -\gamma \mathbf{v} g \left(\frac{\partial^2 n}{\partial x^2} + \frac{\partial^2 n}{\partial y^2} \right) + \frac{\mu}{\rho} \nabla^4 w, \tag{3.4b}$$

$$\frac{\partial n}{\partial t} = \Theta \nabla^2 n - w \frac{dN_0}{dz} - W_c \frac{\partial n}{\partial z}, \tag{3.4c}$$

where ζ denotes the z-component of $\boldsymbol{\eta}$.

Equation (3.4) constitute the linearized perturbed system. We now seek solutions to these equations that satisfy the appropriate boundary conditions. Regardless of the nature of the bounding surfaces, we require

$$w = 0, \qquad \Theta \frac{\partial n}{\partial z} - W_c n = 0 \qquad \text{on } z = 0, H.$$

Since linear stability analysis focuses on the short-term evolution of small perturbations, it is reasonable to adopt simplifying assumptions that facilitate analytical tractability. In particular, we assume that perturbations in the concentration of microorganisms at the boundaries remain negligible over this timescale. This allows us to impose Dirichlet-type boundary conditions on the concentration perturbations:

$$w = 0, \qquad n = 0 \qquad \text{on } z = 0, H. \tag{3.5}$$

Under the assumption that the boundaries are free, we further impose

$$\frac{\partial^2 w}{\partial z^2} = 0, \qquad \frac{\partial \zeta}{\partial z} = 0, \tag{3.6}$$

whereas if the boundaries are assumed to be rigid, we require

$$\frac{\partial w}{\partial z} = 0, \qquad \zeta = 0. \tag{3.7}$$

In the analysis that follows below, free boundary conditions are assumed.

This simplification reduces the complexity of the eigenvalue problem and enables explicit determination of eigenfunctions, which is essential for deriving stability criteria. Although these assumptions may not fully capture long-term dynamics near the boundaries, they provide valuable insight into the onset of instability and the initial growth of perturbations, which are the principal objectives of this analysis.

Finally, we observe that the vorticity equation (3.4a) decouples from those governing the vertical velocity and concentration. It can therefore be analyzed independently as a characteristic problem, whose eigenvalue is always negative. Consequently, in what follows we restrict our attention to the reduced system consisting of the vertical velocity w (3.4b) and the concentration perturbation n (3.4c).

3.2. Non-dimensionalization. In order to facilitate the analysis, we first non-dimensionalize the governing equations. All lengths are scaled by the layer depth H, time by the diffusive timescale H^2/Θ, fluid velocity by the swimming speed W_c, and concentration by the mean density $\overline{N}$. Dimensionless variables are denoted with a superscript *.

Substituting these scalings into (3.4b) and (3.4c) yields

$$\frac{\partial}{\partial t^*}\nabla^2 w^* = -\frac{\gamma \mathbf{v} g H^2 \overline{N}}{W_c \Theta}\left(\frac{\partial^2 n^*}{\partial x^{*2}} + \frac{\partial^2 n^*}{\partial y^{*2}}\right) + \frac{\nu}{\Theta}\nabla^4 w^*,$$

$$\frac{\partial n^*}{\partial t^*} = \nabla^2 n^* - \frac{W_c H}{\Theta}\frac{dN_0^*(z^*)}{dz^*}\, w^* - \frac{W_c H}{\Theta}\frac{\partial n^*}{\partial z^*}.$$

The horizontal boundaries are now located at $z^* \in \{0, 1\}$. In dimensionless form, the steady-state concentration profile is

$$N_0^*(z^*) = \frac{W_c H}{\Theta}\,\frac{1}{\exp\left(\frac{W_c H}{\Theta}\right) - 1}\,\exp\left(\tfrac{W_c H}{\Theta} z^*\right).$$

We introduce the key non-dimensional parameters in Table 3.1. Dropping the asterisks

TABLE 3.1
Non-dimensional Parameters.

Schmidt number	$Sc = \dfrac{\nu}{\Theta}$
Péclet number	$Pe = \dfrac{W_c H}{\Theta}$

for notational simplicity, the system reduces to

$$\begin{aligned} \frac{\partial}{\partial t}\nabla^2 w &= -\frac{\gamma \mathbf{v} g H^2 \overline{N}}{W_c \Theta}\left(\frac{\partial^2 n}{\partial x^2} + \frac{\partial^2 n}{\partial y^2}\right) + Sc\nabla^4 w, \\ \frac{\partial n}{\partial t} &= \nabla^2 n - Pe\frac{dN_0(z)}{dz} w - Pe\frac{\partial n}{\partial z}. \end{aligned} \tag{3.8}$$

$$N_0(z) = Pe\,\frac{1}{\exp(Pe) - 1}\,\exp(Pe\, z). \tag{3.9}$$

3.3. Linear Stability Analysis: Eigenvalue Problem. We analyze the stability of perturbations by employing a normal mode approach, in which disturbances are represented as periodic waves with assigned wave numbers in the horizontal directions. Specifically, we set

$$\begin{aligned} w(x, y, z, t) &= W(t, z)\, e^{i(k_x \pi x + k_y \pi y)}, \\ n(x, y, z, t) &= N(t, z)\, e^{i(k_x \pi x + k_y \pi y)}, \end{aligned}$$

where $k\pi = \sqrt{(k_x\pi)^2 + (k_y\pi)^2}$ denotes the total horizontal wavenumber.

Substituting these forms into the nondimensional governing equations (3.8) yields the coupled linearized system

$$\left(\tfrac{d^2}{dz^2} - k^2\pi^2\right)\left[Sc\left(\tfrac{d^2}{dz^2} - k^2\pi^2\right) - \tfrac{d}{dt}\right] W(t, z) = -\frac{\gamma v g H^2 \overline{N}}{W_c \Theta}\, k^2\pi^2 N(t, z), \tag{3.10}$$

$$\left(\tfrac{d^2}{dz^2} - Pe\tfrac{d}{dz} - k^2\pi^2 - \tfrac{d}{dt}\right) N(t, z) = Pe\tfrac{dN_0(z)}{dz}\, W(t, z), \tag{3.11}$$

together with boundary conditions:

$$W(t,z) = \tfrac{d^2W(t,z)}{dz^2} = N(t,z) = 0, \quad z = 0, 1.$$

Eliminating $N(t,z)$ between (3.10) and (3.11) produces a single sixth-order ordinary differential equation with non-constant coefficients:

$$\begin{aligned}&\left(\tfrac{d^2}{dz^2} - Pe\tfrac{d}{dz} - k^2\pi^2 - \tfrac{d}{dt}\right)\left(\tfrac{d^2}{dz^2} - k^2\pi^2\right)\left(\tfrac{d^2}{dz^2} - k^2\pi^2 - \tfrac{1}{Sc}\tfrac{d}{dt}\right)W(t,z)\\ &\quad = -\frac{Pe}{Sc}\,\frac{\gamma v g H^2 \overline{N}}{W_c \Theta}\, k^2\pi^2 \tfrac{dN_0(z)}{dz}\, W(t,z).\end{aligned}$$

Substituting the steady-state concentration profile $N_0(z)$ from (3.9) gives the explicit form:

$$\begin{aligned}&\left(\tfrac{d^2}{dz^2} - Pe\tfrac{d}{dz} - k^2\pi^2 - \tfrac{d}{dt}\right)\left(\tfrac{d^2}{dz^2} - k^2\pi^2\right)\left(\tfrac{d^2}{dz^2} - k^2\pi^2 - \tfrac{1}{Sc}\tfrac{d}{dt}\right)W(t,z)\\ &\quad = -\frac{\gamma v g H^2 \overline{N}}{W_c \nu}\,\frac{Pe^3}{\exp(Pe) - 1}\, k^2\pi^2 \exp(Pez)\, W(t,z),\end{aligned} \tag{3.12}$$

subject to boundary conditions:

$$W(t,z) = \tfrac{d^2W(t,z)}{dz^2} = \left(\tfrac{d^2}{dz^2} - k^2\pi^2\right)\left(\tfrac{d^2}{dz^2} - k^2\pi^2 - \tfrac{1}{Sc}\tfrac{d}{dt}\right)W(t,z) = 0, \quad z = 0, 1. \tag{3.13}$$

To proceed, we assume separability of space and time and set $W(t,z) = e^{\lambda t}\hat{W}(z)$. Under this assumption, equation (3.12) becomes an eigenvalue problem for $\hat{W}(z)$, with the temporal dependence contained entirely in the exponential factor.

Expanding the last boundary condition in (3.13), it follows that

$$\tfrac{d^4\hat{W}}{dz^4}(z) = 0, \quad z = 0, 1.$$

Differentiating the last condition twice yields:

$$\tfrac{d^6\hat{W}}{dz^6}(z) = 0, \quad z = 0, 1.$$

By induction, all even-order derivatives of $\hat{W}$ vanish at the endpoints:

$$\tfrac{d^{(2m)}\hat{W}}{dz^{(2m)}} = 0, \quad z = 0, 1, \quad m = 1, 2, 3, \ldots$$

This condition implies that the eigenfunctions must satisfy homogeneous even - derivative boundary conditions, which are naturally satisfied by sine functions. Therefore, $\hat{W}(z)$ admits a Fourier sine series expansion, and we express the concentration function as:

$$W(t,z) = \sum_{n=1}^{\infty} A_n e^{\lambda_n t} \sin(n\pi z), \tag{3.14}$$

where λ_n denotes the growth rate associated with the nth mode, and A_n is the corresponding amplitude.

Substituting this expansion into equation (3.12), we have:

$$\begin{aligned}&\sum_{n=1}^{\infty}\left(\tfrac{d^2}{dz^2} - Pe\tfrac{d}{dz} - k^2\pi^2 - \tfrac{d}{dt}\right)\left(\tfrac{d^2}{dz^2} - k^2\pi^2\right)\left(\tfrac{d^2}{dz^2} - k^2\pi^2 - \tfrac{1}{Sc}\tfrac{d}{dt}\right)e^{\lambda_n t}\sin(n\pi z)\\ &\quad = -\frac{\gamma v g H^2 \overline{N}}{W_c \nu}\,\frac{Pe^3}{\exp(Pe) - 1}\, k^2\pi^2 \exp(Pez) \sum_{n=1}^{\infty} e^{\lambda_n t}\sin(n\pi z).\end{aligned} \tag{3.15}$$

4. Analytical Stability Criterion under Constant Drift Approximation.

4.1. General method. A key difficulty in the linear stability analysis arises from the spatially varying coefficient $\exp(Pez)$ in equation (3.15), originating from the vertical gradient of the steady-state concentration profile $\frac{dN_0(z)}{dz}$. This exponential dependence couples Fourier modes in the vertical direction, which complicates the analytical treatment of the eigenvalue problem and obstructs explicit derivations of growth rates.

To mitigate this difficulty, we employ a **constant drift approximation**, in which the exponential term is replaced by a representative constant:

$$\exp(Pe\, z) \approx a, \tag{4.1}$$

where a characterizes the effective drift strength in a simplified but analytically tractable form.

This approximation preserves the structure of the governing eigenvalue problem while removing spatial variability in the drift term. The constant a may be selected according to specific points in the domain (bottom, top, center) or by its spatial average. Although such a simplification introduces an approximation error, it enables explicit stability conditions and reveals how spatial variation in drift strength influences the dynamics.

The choice of a directly controls the destabilizing term. Since $\exp(Pez)$ is strictly increasing on $[0,1]$, larger a (e.g., the top value) corresponds to stronger effective drift and more pessimistic stability thresholds (lower bounds). In contrast, smaller a (e.g., the bottom value) yields more optimistic thresholds (upper bounds). By systematically varying a, we bound the true stability threshold and quantify sensitivity to this approximation.

We now present the analytical derivation under this constant approximation, followed by a detailed investigation of several representative choices of a that bracket the stability behavior.

Substituting (4.1) into (3.15) gives

$$\begin{aligned}\sum_{n=1}^{\infty}\Big(\tfrac{d^2}{dz^2} - Pe\,\tfrac{d}{dz} - k^2\pi^2 - \tfrac{d}{dt}\Big)\Big(\tfrac{d^2}{dz^2} - k^2\pi^2\Big)\Big(\tfrac{d^2}{dz^2} - k^2\pi^2 - \tfrac{1}{Sc}\tfrac{d}{dt}\Big)e^{\lambda_n t}\sin(n\pi z)\\ = -\,a\,\frac{\gamma \mathbf{v} g H^2 \overline{N}}{W_c \nu}\,\frac{Pe^3}{\exp(Pe)-1}\,k^2\pi^2\sum_{n=1}^{\infty} e^{\lambda_n t}\sin(n\pi z).\end{aligned} \tag{4.2}$$

Projecting (4.2) onto $\sin(n\pi z)$ and using orthogonality yields the modal equation:

$$\big[\,n^2\pi^2 + k^2\pi^2 + \lambda_n\,\big]\big[\,Sc\,(n^2\pi^2 + k^2\pi^2) + \lambda_n\,\big] = a\,\frac{\gamma \mathbf{v} g H^2 \overline{N}}{W_c \Theta}\,\frac{Pe^3}{\exp(Pe)-1}\,\frac{k^2\pi^2}{n^2\pi^2 + k^2\pi^2}. \tag{4.3}$$

This leads to the following quadratic equation for the growth rate λ_n:

$$\begin{aligned}\lambda_n^2 + (Sc+1)\left(n^2\pi^2 + k^2\pi^2\right)\lambda_n + Sc\left(n^2\pi^2 + k^2\pi^2\right)^2\\ -\,a\,\frac{\gamma \mathbf{v} g H^2 \overline{N}}{W_c \Theta}\,\frac{Pe^3}{\exp(Pe)-1}\,\frac{k^2\pi^2}{n^2\pi^2 + k^2\pi^2} \;=\; 0.\end{aligned} \tag{4.4}$$

Since the discriminant is always positive, two distinct real roots exist. The quadratic opens upward, and its axis lies at a negative λ_n, ensuring that one root is

negative. Stability requires both roots to be negative, which holds precisely when the constant term is positive. Hence stability demands

$$Sc\left(n^2\pi^2+k^2\pi^2\right)^2 - a\,\frac{\gamma \mathbf{v} g H^2 \overline{N}}{W_c \Theta}\,\frac{Pe^3}{\exp(Pe)-1}\,\frac{k^2\pi^2}{n^2\pi^2+k^2\pi^2} > 0, \quad \forall\, n,k \in \mathbb{Z}^+.$$

Equivalently,

$$a\,\frac{\gamma \mathbf{v} g H^3 \overline{N}}{\nu \Theta}\,\frac{Pe^2}{\exp(Pe)-1} < \frac{\left(n^2\pi^2+k^2\pi^2\right)^3}{k^2\pi^2}, \quad \forall\, n,k \in \mathbb{Z}^+.$$

The minimum of the right-hand side occurs at $n=k=1$, yielding the global stability condition

$$a\,\frac{\gamma \mathbf{v} g H^3 \overline{N}}{\nu \Theta}\,\frac{Pe^2}{\exp(Pe)-1} \;<\; 8\pi^4. \tag{4.5}$$

Rayleigh number interpretation. This naturally motivates defining a *bioconvection Rayleigh number* under the constant approximation:

$$Ra_{bio}(a) \;=\; a\,\frac{\gamma \mathbf{v} g H^3 \overline{N}}{\nu \Theta}\,\frac{Pe^2}{\exp(Pe)-1}. \tag{4.6}$$

so the stability condition succinctly reads

$$Ra_{bio}(a) \;<\; Ra_{bio-critical}, \qquad \text{with} \qquad Ra_{bio-critical} \;=\; 8\pi^4. \tag{4.7}$$

4.2. Summary of Approximation Choices. In the remainder of this section, we examine representative choices of a (bottom, top, mid-height, and average values). These approximations will allow us to:

- derive explicit expressions for $Ra_{bio}(a)$ under each approximation,
- quantify sensitivity of stability thresholds to the drift profile, and
- establish bounds on critical system parameters such as the minimum container height H required to maintain stability.

Table 4.1 summarizes the five approximations and the associated stability criteria.

TABLE 4.1
Constant approximations a for $\exp(Pe\,z)$ and the corresponding stability conditions.

Approx. type	**Value of a**	**Stability condition**
Top value	$\exp(Pe)$	$\exp(Pe)\,\frac{\gamma \mathbf{v} g H^3 \overline{N}}{\nu \Theta}\,\frac{Pe^2}{\exp(Pe)-1} < 8\pi^4$
Bottom value	1	$\frac{\gamma \mathbf{v} g H^3 \overline{N}}{\nu \Theta}\,\frac{Pe^2}{\exp(Pe)-1} < 8\pi^4$
Spatial avg.	$\frac{\exp(Pe)-1}{Pe}$	$Pe\,\frac{\gamma \mathbf{v} g H^3 \overline{N}}{\nu \Theta} < 8\pi^4$
Mid-height	$\exp(Pe/2)$	$\exp(Pe/2)\,\frac{\gamma \mathbf{v} g H^3 \overline{N}}{\nu \Theta}\,\frac{Pe^2}{\exp(Pe)-1} < 8\pi^4$
Endpoint avg.	$\frac{1+\exp(Pe)}{2}$	$\frac{1+\exp(Pe)}{2}\,\frac{\gamma \mathbf{v} g H^3 \overline{N}}{\nu \Theta}\,\frac{Pe^2}{\exp(Pe)-1} < 8\pi^4$

To complement the analytical stability criteria derived above, Figure 4.1 summarizes the results obtained under the constant approximation. Panel (a) demonstrates

how several constant choices bracket the exponential drift profile, offering a structured means to explore upper and lower bounds as well as intermediate scenarios, panel (b) shows how the resulting bioconvection Rayleigh number depends on the upswimming velocity W_c, and panel (c) maps the stability boundary in the (H, W_c) plane, highlighting the combined influence of swimming speed and container depth.

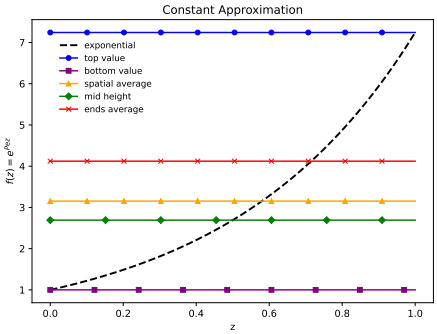

(a) Constant approximations.

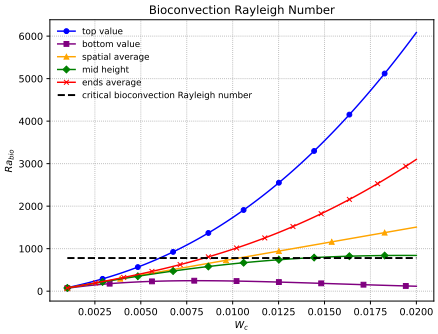

(b) Ra_{bio} vs. W_c.

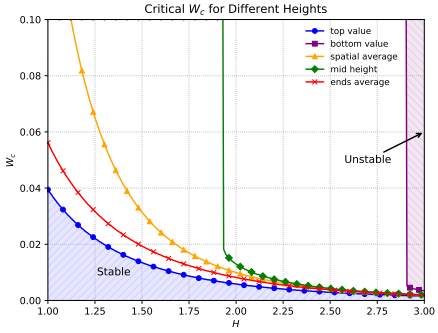

(c) Stability in (H, W_c).

FIG. 4.1. *Analytical results under the constant approximation.*
(a) Exponential drift profile $f(z) = \exp(Pe\, z)$ *(dashed black line) with five representative constant approximations: bottom* ($a = 1$, *purple squares), top* ($a = \exp(Pe)$, *blue circles), spatial average* ($a = \frac{\exp(Pe)-1}{Pe}$, *orange triangles), mid-height* ($a = \exp(\frac{1}{2}Pe)$, *green diamonds), and endpoint average* ($a = \frac{1+\exp(Pe)}{2}$, *red crosses).*
(b) Bioconvection Rayleigh number Ra_{bio} *as a function of upswimming velocity* W_c *under these approximations; the horizontal dashed black line at* $8\pi^4$ *indicates the critical threshold.*
(c) Stability diagram in the (H, W_c) *plane. The purple region corresponds to guaranteed instability* ($a = \exp(Pe)$), *the blue region to guaranteed stability* ($a = 1$), *while intermediate curves reflect the sensitivity to approximation choices.*

4.3. Lower Bound Estimate. To derive a conservative estimate of the stability threshold, we adopt the largest value of the exponential term in the domain, namely its value at the top boundary (the solid line with circles, blue in Figure 4.1a):

$$a = \exp(Pe).$$

This corresponds to the strongest effective drift and hence maximizes the destabilizing effect of cell aggregation. If stability is maintained under this unfavorable scenario, it is guaranteed under the true, spatially varying profile. This choice of a corresponds to the "shallow water" case commonly considered in the literature [11, 30].

Using the definition of the bioconvective Rayleigh number in (4.6), the criterion becomes

$$Ra_{bio}^{(\text{lower})} = \exp(Pe)\,\frac{\gamma \mathbf{v} g H^3 \overline{N}}{\nu \Theta}\,\frac{Pe^2}{\exp(Pe)-1} < 8\pi^4.$$

Figure 4.1b illustrates this condition: the *top-value approximation* (solid blue line with circle markers) shows how Ra_{bio} varies with the upswimming velocity W_c, and the intersection with the horizontal dashed line marks the onset of instability. Figure 4.1c further shows the dependence on suspension height. The region labeled *Stable* (blue shading) corresponds to parameter values where the system remains stable under this lower-bound estimate. Stability in this region is thus guaranteed, given the conservative nature of this approximation.

4.4. Upper Bound Estimate. Conversely, for an optimistic estimate of the threshold, we take the smallest value of the exponential term, namely its bottom boundary value (the solid purple line with squares in Figure 4.1a):

$$a = \exp(0) = 1.$$

This corresponds to the weakest effective drift, minimizing the destabilizing effect of cell aggregation. Consequently, the resulting stability condition serves as a rigorous upper bound on the true threshold: if instability is predicted under this most favorable scenario, it must also occur for the actual system with spatially varying drift.

The resulting stability condition reads

$$Ra_{bio}^{(\text{upper})} = \frac{\gamma \mathbf{v} g H^3 \overline{N}}{\nu \Theta}\,\frac{Pe^2}{\exp(Pe)-1} < 8\pi^4.$$

As shown in Figure 4.1b, the *bottom-value approximation* (solid purple line with square markers) intersects the dashed critical line at a higher W_c compared to the lower-bound case, reflecting the optimistic nature of this estimate. In the (W_c, H)-plane (Figure 4.1c), the region labeled *Unstable* (purple shading) indicates combinations that are unstable even under this most optimistic approximation. This means if parameters fall within this region, instability is guaranteed even under the least destabilizing approximation, thus ensuring that these conditions robustly lead to the onset of bioconvective patterns.

4.5. Intermediate Estimates. Beyond the rigorous upper and lower bounds, we also investigate several intermediate choices of the constant a to furnish a more balanced approximation that captures the average influence of the non-uniform drift. Each provides a different perspective on the effective strength of the drift term and helps systematically bracket the true stability condition.

Spatial average. A natural choice is the spatial average of the exponential profile across the domain:

$$a = \int_0^1 \exp(Pe\, z)\, dz = \frac{\exp(Pe)-1}{Pe}.$$

This integrates the contribution of drift over the entire suspension height. The corresponding Rayleigh number is

$$Ra_{bio}^{(\text{avg})} = \frac{\exp(Pe)-1}{Pe}\,\frac{\gamma \mathbf{v} g H^3 \overline{N}}{\nu \Theta}\,\frac{Pe^2}{\exp(Pe)-1} = Pe\,\frac{\gamma \mathbf{v} g H^3 \overline{N}}{\nu \Theta},$$

leading to the stability condition

$$Pe\,\frac{\gamma \mathbf{v} g H^3 \overline{N}}{\nu \Theta} < 8\pi^4.$$

This case corresponds to the solid orange line with triangle markers in Figure 4.1.

Mid-height value. Another intermediate choice is the value at the midpoint of the domain:

$$a = \exp\left(\tfrac{1}{2}Pe\right).$$

This yields

$$Ra_{bio}^{(\mathrm{mid})} = \exp\left(\tfrac{1}{2}Pe\right)\,\frac{\gamma \mathbf{v} g H^3 \overline{N}}{\nu \Theta}\,\frac{Pe^2}{\exp(Pe)-1},$$

with stability condition

$$\exp\left(\tfrac{1}{2}Pe\right)\,\frac{\gamma \mathbf{v} g H^3 \overline{N}}{\nu \Theta}\,\frac{Pe^2}{\exp(Pe)-1} < 8\pi^4.$$

This is shown by the solid green line with diamond markers in Figure 4.1.

Endpoint average. Finally, we take the arithmetic mean of the top and bottom boundary values:

$$a = \tfrac{1}{2}\left(1+\exp(Pe)\right).$$

This "endpoint average" represents a simple balance between the strongest and weakest drift influences, leading to

$$Ra_{bio}^{(\mathrm{end})} = \tfrac{1}{2}\left(1+\exp(Pe)\right)\,\frac{\gamma \mathbf{v} g H^3 \overline{N}}{\nu \Theta}\,\frac{Pe^2}{\exp(Pe)-1},$$

and the corresponding stability condition

$$\tfrac{1}{2}\left(1+\exp(Pe)\right)\,\frac{\gamma \mathbf{v} g H^3 \overline{N}}{\nu \Theta}\,\frac{Pe^2}{\exp(Pe)-1} < 8\pi^4.$$

This case is plotted as the the solid red line with cross markers in Figure 4.1.

Together, these intermediate approximations provide explicit analytical criteria that interpolate between the conservative lower and optimistic upper bounds. In section 6, we will compare these predictions with direct numerical simulations to evaluate their sharpness and practical utility.

5. Numerical Determination of Stability Thresholds. The analytical criteria derived in section 4 provide rigorous bounds on the onset of instability but rely on simplified constant approximations of the drift term. These estimates inevitably neglect certain nonlinear interactions and spatial variations present in the full system. To complement the analytical approach, we now turn to direct numerical simulations of the coupled bioconvection equations. Our objectives are twofold: (i) to determine stability thresholds without approximation of the drift profile, and (ii) to compare these results with the analytical predictions in order to assess their sharpness.

We begin by describing the numerical discretization and the criterion used to classify solutions as stable or unstable. We then introduce a bisection algorithm for efficiently locating critical parameter values, and illustrate the procedure by computing the critical up-swimming velocity for a fixed container height. Finally, we extend the computations across a range of heights to map the full stability boundary in the (H, W_c) plane.

5.1. Numerical procedure and stability criterion. We solve the full coupled system (2.1) using the second-order partitioned time-stepping finite element scheme introduced in [14]. The spatial discretization employs P_2 elements for velocity and P_1 elements for both concentration and pressure, on meshes with resolution $\Delta x = 0.05\,\text{cm}$. A fixed time step of $\Delta t = 0.01\,\text{s}$ is used throughout. All computations were carried out in the Julia programming language [7] using the Gridap finite element library [3, 39], together with GridapSolvers [27] and the `DataStructures.jl` package [19].

Stability of a given parameter configuration is assessed as follows:

- **Initial state.** The system is initialized at the exponential steady state (2.6)–(2.8), which serves as the unperturbed base state.
- **Perturbation.** Small random perturbations of order $\mathcal{O}(10^{-3})$ are added independently at each mesh node to both velocity and concentration fields, with zero net sum to preserve mass and momentum.
- **Time evolution.** The system is advanced up to $T = 1400\,\text{s}$, a horizon sufficient for instabilities to emerge if present.
- **Classification.** In principle, stability could be assessed by comparing the final state with the initial exponential profile. However, interpolation errors in representing the exponential steady state on a discrete mesh introduce spurious deviations that make a purely norm-based criterion unreliable. In practice, we therefore classify outcomes by visual inspection: simulations are deemed *unstable* if characteristic finger-like plumes emerge by $T = 1400\,\text{s}$, and *stable* otherwise.

Each individual simulation, on average, requires approximately 40 CPU-hours on a standard desktop processor. While this makes brute-force parameter sweeps infeasible, our approach is sufficiently accurate and robust for assessing stability. To balance reliability with efficiency, we employ a targeted bisection strategy, described in the next subsection, which reduces the number of simulations needed while still yielding trustworthy critical thresholds.

Algorithm 5.1 Bisection search for stability threshold

Inputs: interval $[x_{\min}, x_{\max}]$, tolerance ϵ; all other fixed parameters
Run simulations at $x_{\min}$ and $x_{\max}$ to confirm one stable and one unstable
while $|x_{\max} - x_{\min}| > \epsilon$ **do**
  $x \leftarrow \frac{1}{2}(x_{\min} + x_{\max})$
  Run simulation at x
  if stable **then**
    $x_{\min} \leftarrow x$
  else
    $x_{\max} \leftarrow x$
  end if
end while
return $x_c \leftarrow \frac{1}{2}(x_{\min} + x_{\max})$

5.2. Bisection algorithm for identifying stability thresholds. To locate the critical value of a single parameter (e.g., W_c) marking the transition between stable and unstable behavior, we vary only that parameter while holding all others fixed at baseline values. An initial interval $[x_{\min}, x_{\max}]$ is chosen from physically relevant ranges or guided by the analytical estimates in Section 4. Simulations at the

endpoints verify that one outcome is stable and the other unstable, ensuring that the threshold is bracketed.

The interval is then iteratively refined: at each step the midpoint is tested, and the interval is updated according to the stability outcome. The process continues until the interval length falls below a prescribed tolerance ϵ, at which point the midpoint is taken as the approximate critical value.

This procedure is general and can be applied to any of the model parameters. It is summarized in Algorithm 5.1. In the next subsection, we illustrate the method by applying it to determine the critical up-swimming velocity W_c under a fixed set of baseline parameters.

5.3. Example: determining the critical up-swimming velocity. As an illustration of the bisection method, we compute the critical upswimming velocity W_c while keeping all other parameters fixed at representative baseline values. This example is directly motivated by applications such as wastewater treatment, where bioconvection enhances mixing and transport. In practice, if expected convection patterns do not develop under given operating conditions, for example, due to microorganisms having insufficient swimming speeds, operators could address this by introducing species with higher up-swimming velocities. By quantifying the critical threshold, our results provide a predictive tool to guide such adjustments and ensure the desired level of bioconvective mixing is achieved.

TABLE 5.1
Baseline values of the model parameters used in the stability computations, with only the up-swimming velocity W_c varied.

Parameter	**Value**
H (container height)	2.0 cm
μ (dynamic viscosity)	0.01 g/cm/s
ρ (density of culture fluid)	1.0 g/cm^3
γ (microorganism density ratio)	$5 \cdot 10^{-10}$
$\mathbf{v}$ (cell volume)	1.0 cm^3
Θ (diffusion rate of microorganism)	0.01 cm^2/s
$\overline{N}$ (average cell concentration)	10^4 /cm^3

We apply the bisection algorithm to $W_c \in [0.001, 0.1]$ cm/s, an interval chosen to reflect typical experimental swimming speeds, observed in experimental studies [31]. A tolerance of $\epsilon = 0.0002$ is imposed, requiring 10 simulations to converge. All other parameters are fixed at the baseline values in Table 5.1.

Figure 5.1 shows the sequence of simulations performed during this procedure, plotted in the (H, W_c) plane. Since H is fixed, the results appear as a vertical slice, with stable cases marked by dots and unstable cases by crosses. The vertical dashed line marks the chosen height. The midpoint of the final bracket gives the approximate threshold value $W_c^* = 0.0051$ at which the system transitions from stable to unstable.

Below this threshold, perturbations decay and the suspension remains close to the exponential steady state; above it, plume-like instabilities grow and dominate the flow. This example demonstrates how the bisection method efficiently isolates critical parameters while avoiding the cost of exhaustive parameter sweeps.

5.4. Numerical stability condition. We now extend the analysis by systematically mapping the stability boundary in the (H, W_c) plane. While the previous

subsection illustrated our procedure at a fixed container height, here we vary H over the range $[1, 3]$ cm in increments of $\Delta H = 0.1$ cm. At each height, we apply the same bisection algorithm to determine the critical up-swimming velocity W_c^* that separates stable from unstable regimes.

This procedure yields a discrete set of critical points $\{(H, W_c^*)\}$, which we interpolate to obtain a numerical stability curve. The result is shown in Figure 5.2. Parameter combinations below the curve correspond to stable suspensions, while those above lead to plume formation and instability.

A detailed comparison between this numerically determined stability condition and the analytical bounds derived in section 4 is presented in section 6.

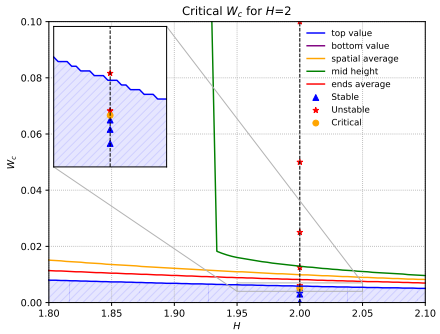

FIG. 5.1. *Results of the bisection procedure at fixed container height $H = 2.0$ cm, used to determine the critical up-swimming velocity W_c^*. Stable simulations are marked with dots, unstable simulations with crosses, and the vertical dashed line highlights the chosen height.*

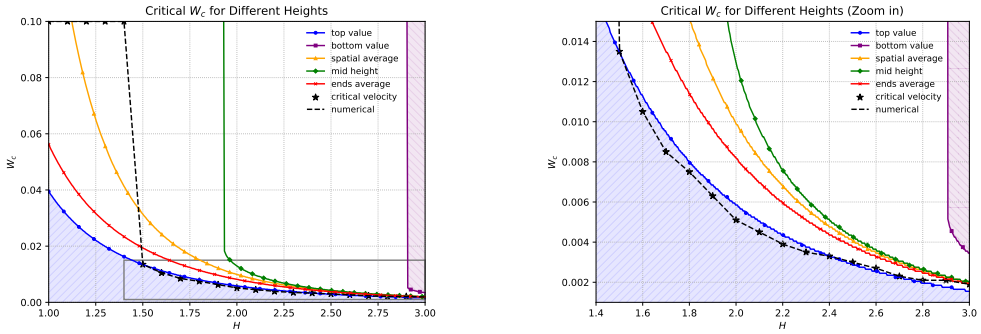

FIG. 5.2. *Numerically determined stability condition in the (H, W_c) plane. Critical velocities W_c^* (stars) are computed at each height using bisection, and the linear interpolated curve separates stable (below) from unstable (above) regimes.*

6. Discussion. We studied the stability of a bioconvective suspension driven by biased swimming microorganisms, using a combination of analytical and numerical approaches. Our linear stability analysis yields explicit formulas for the critical conditions. By retaining the full Péclet dependence in the Rayleigh number, it also clarifies how drift strength influences the onset of instability. This formulation recovers the known asymptotic limits and extends them to general parameter regimes. Time-dependent simulations were employed to compute numerical thresholds and evaluate

the sharpness of the analytical predictions, from which the most accurate approximations were identified. The combined analytical–numerical framework provides a practical tool for predicting flow transitions in bioconvective systems and related applications. This framework can be extended to analyze stability in a wide range of biofluid systems where cell–fluid coupling plays a central role.

The bioconvective Rayleigh number (4.6) was derived through linear stability analysis about the steady state with zero velocity. A key difficulty arises from the non-constant coefficient $\exp Pe\, z$, which introduces explicit dependence on the Péclet number Pe. Earlier studies avoided this complication by assuming either $Pe \ll 1$ or $Pe \gg 1$, yielding Rayleigh numbers that are independent of Pe [11, 30]. In realistic bioconvective systems, however, the drift intensity typically satisfies $Pe = \mathcal{O}(1)$, and the corresponding stability condition must retain this dependence. To address this, we preserve the full $Pe-$dependence and approximate the nonlinear drift term by a representative effective value. While this approximation introduces some modeling error, it extends prior asymptotic results and offers new quantitative insight into how the drift strength influences the onset of instability.

The linear theory yields explicit criteria for instability, but it neglects nonlinear interactions and therefore describes only the initial growth regime. As perturbations evolve, nonlinear effects become significant and the analytical predictions gradually deviate from observed thresholds. Our direct numerical simulations compensate for this limitation by resolving the full time-dependent dynamics. Although computationally intensive, these simulations provide definitive stability thresholds and enable quantitative assessment of the analytical predictions.

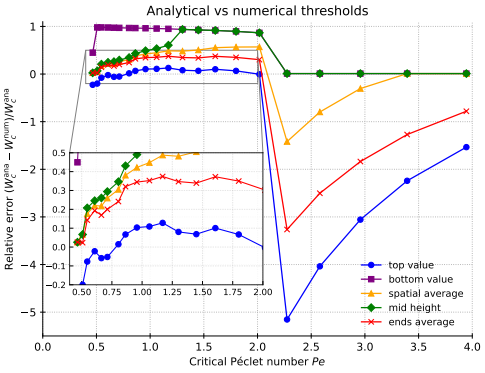

FIG. 6.1. *Relative error between analytical and numerical critical velocities as a function of Péclet number Pe. Each curve corresponds to a different drift-term approximation.*

Small $Pe \ll 1$. In the weak-advection regime, our formulation reproduces the classical result of Childress et al., corresponding to the top-value approximation (blue curve) in Figure 6.1. This estimate slightly overpredicts the stabilizing effect of the drift term, resulting in a systematic overshoot of the critical velocity. Intermediate approximations yield tighter bounds and align more closely with numerical thresholds, indicating that the local averaging better represents the effective drift strength at small Pe.

Moderate $Pe = \mathcal{O}(1)$. For moderate Péclet numbers, the top-value approximation performs best, maintaining a relative error within about 10% of the numerical results. Linear analysis confirms that this estimate defines a guaranteed stable region. How-

ever, direct simulations reveal weak instabilities within this nominally stable domain (Figure 5.2). Near criticality, the temporal growth rate λ is nearly zero, delaying the visible onset of pattern formation. As time evolves, nonlinear effects become dominant, leading to eventual flow development even where the linear theory predicts stability. This highlights again the importance of the numerical simulations.

Large $Pe \gg 1$. For strong advection, the top-value approximation and most averaged approximations lose accuracy, exhibiting a sharp increase in relative error around $Pe \approx 2$ (advection dominates diffusion in this case). The subsequent recovery stems from the imposed physical upper bound on the swimming velocity: the numerical critical velocity saturates at a finite value. In contrast, the bottom-value approximation, which defines the analytical upper bound, correctly delineates the guaranteed unstable region. However, numerical results indicate that the mid-point estimate also yields the same relative error. This observation suggests that the analytical instability bounds can be modestly extended toward the mid-point value for large Pe, offering improved predictive capability.

Future work will extend the present results beyond the linear regime. Nonlinear stability analysis and more efficient numerical schemes are needed to better characterize the system dynamics. Data-driven and reduced-order models may further accelerate the identification of stability thresholds, while simplified Lorenz-type models, motivated by the analogy with Rayleigh-Bénard convection, may offer additional insight into the system.

7. Appendices. The study of bioconvection relies on mathematical models that connect the microscopic behavior of swimming microorganisms to the macroscopic motion of the surrounding fluid. These processes are represented by **partial differential equations (PDEs)**, which describe how quantities such as cell concentration and velocity evolve over time and space. PDE models capture both the transport of cells (through swimming and diffusion) and the fluid motion (through the Navier–Stokes equations), linking biological activity to measurable flow patterns.

To understand when a suspension begins to move and form patterns, we use **stability analysis**, a mathematical framework for studying how small disturbances evolve over time. This approach provides analytical conditions that predict when a system transitions from a motionless state to one with organized flow. Complementing this, we perform **numerical simulations** to determine the corresponding thresholds computationally. In this work, we employ **finite element methods (FEM)**, which divide the physical domain into small spatial elements and the time into discrete intervals, allowing the governing equations to be solved on a computer. These simulations act like virtual experiments, reproducing the biological process computationally rather than with real organisms. By systematically adjusting parameters through a **bisection search**, we identify the precise numerical conditions that separate stable and unstable regime. Together, these analytical and computational methods provide a way to translate biological mechanisms into predictive, quantitative descriptions of when and how fluid motion emerges in microbial systems.

Further Reading. The following references provide accessible background that forms the foundation for this work.

Biological Background and Mathematical Model.

- Description of bioconvection and early biological explanations of its mechanism. [32]
- Formulation of the continuum model of bioconvection, introducing a coupled system of PDEs for cell transport and fluid motion. [11]

- A comprehensive review that summarizes both experimental observations and theoretical developments in bioconvective systems. [17]

Mathematical Foundations of Stability Analysis.

- General introductions to linear stability analysis, explaining how small disturbances to a steady state can grow or decay and how this predicts the onset of new flow patterns. [29]

Numerical Simulations and Bisection Method.

- An introduction to the finite element method. [41]
- A detailed implementation of a finite element scheme for simulating bioconvection. [14]
- Descriptions of basic root-finding algorithms, such as the bisection method, which are used here to locate the critical parameter values separating stable and unstable regimes. [22]

8. Declarations.

Authorship and Contributorship Statement. All authors have made substantial intellectual contributions to the design, modeling, analysis, numerical simulations and interpretation of the work, and have read and approved the final manuscript. In addition, the following contributions occurred: Conceptualization: Jiabao Nie, Martina Bukač, Catalin Trenchea; Methodology: Jiabao Nie, Martina Bukač, Catalin Trenchea; Formal analysis and investigation: Jiabao Nie; Writing - original draft preparation: Jiabao Nie; Writing - review and editing: Jiabao Nie, Martina Bukač, Catalin Trenchea; Supervision: Martina Bukač, Catalin Trenchea.

Conflicts of Interest. The authors declare there are no conflicts of interest.

Data and Code Availability Statement. The source code and input files used to generate all figures and numerical results in this paper are openly available at https://github.com/Jaybo-Nie/Bioconvection-stability-analysis. This includes the scripts for Figures 4.1, 5.1 and 5.2 as well as the simulation codes used in section 5.

Funding. Martina Bukač is partially supported by the National Science Foundation under grants DMS-2208219 and DMS- 2205695. Catalin Trenchea is partially supported by the National Science Foundation under grant DMS-2208220.

REFERENCES

[1] S. Ahmad, M. Ashraf, and K. Ali, *Bioconvection due to gyrotactic microbes in a nanofluid flow through a porous medium*, Heliyon, 6 (2020), e05832, https://doi.org/10.1016/j.heliyon.2020.e05832.

[2] A. A. Avramenko, Y. Y. Kovetska, and I. V. Shevchuk, *Lorenz approach for analysis of bioconvection instability of gyrotactic motile microorganisms*, Chaos Solitons Fractals, 166 (2023), 112957, https://doi.org/10.1016/j.chaos.2022.112957.

[3] S. Badia and F. Verdugo, *Gridap: An extensible Finite Element toolbox in Julia*, J. Open Source Softw, 5 (2020), 2520, https://doi.org/10.21105/joss.02520.

[4] R. N. Bearon, M. A. Bees, and O. A. Croze, *Biased swimming cells do not disperse in pipes as tracers: A population model based on microscale behaviour*, Phys. Fluids, 24 (2012), 121902, https://doi.org/10.1063/1.4772189.

[5] M. A. Bees, *Advances in Bioconvection*, Annu. Rev. Fluid Mech., 52 (2020), pp. 449–476, https://doi.org/10.1146/annurev-fluid-010518-040558.

[6] M. A. Bees and O. A. Croze, *Mathematics for streamlined biofuel production from unicellular algae*, Biofuels, 5 (2014), pp. 53–65, https://doi.org/10.4155/bfs.13.66.

[7] J. Bezanson, A. Edelman, S. Karpinski, and V. B. Shah, *Julia: A Fresh Approach to Numerical Computing*, SIAM Rev., 59 (2017), pp. 65–98, https://doi.org/10.1137/141000671.

[8] Y. Cao, S. Chen, and H.-W. van Wyk, *Well-posedness and finite element approximation of time dependent generalized bioconvective flow*, Numer. Methods Partial Differential Equations, 36 (2020), pp. 709–733, https://doi.org/10.1002/num.22442.
[9] S. Chandrasekhar, *Hydrodynamic and Hydromagnetic stability*, Courier Corporation, 2013.
[10] F. Charru, *Hydrodynamic Instabilities*, Cambridge University Press, Cambridge, 2011, https://doi.org/10.1017/CBO9780511975172.
[11] S. Childress, M. Levandowsky, and E. A. Spiegel, *Pattern formation in a suspension of swimming microorganisms: equations and stability theory*, J. Fluid Mech., 69 (1975), pp. 591–613, https://doi.org/10.1017/S0022112075001577.
[12] R. de Aguiar, B. Climent-Ezquerra, M. A. Rojas-Medar, and M. D. Rojas-Medar, *On the Convergence of Galerkin Spectral Methods for a Bioconvective Flow*, J. Math. Fluid Mech., 19 (2017), pp. 91–104, https://doi.org/10.1007/s00021-016-0267-4.
[13] P. G. Drazin and W. H. Reid, *Hydrodynamic Stability*, Cambridge University Press, Cambridge, 2nd ed., 2004, https://doi.org/10.1017/CBO9780511616938.
[14] M. Edwards, M. Bukač, and C. Trenchea, *A second-order partitioned method for bioconvective flows with concentration dependent viscosity*, Ann. Math. Sci. Appl., 9 (2024), pp. 141–184, https://doi.org/10.4310/AMSA.2024.v9.n1.a5.
[15] G. P. Galdi and B. Straughan, *Exchange of stabilities, symmetry, and nonlinear stability*, Arch. Rat. Mech. Anal., 89 (1985), pp. 211–228, https://doi.org/10.1007/BF00276872.
[16] S. Ghorai and N. A. Hill, *Gyrotactic bioconvection in three dimensions*, Phys. Fluids, 19 (2007), 054107, https://doi.org/10.1063/1.2731793.
[17] N. A. Hill and T. J. Pedley, *Bioconvection*, Fluid Dyn. Res., 37 (2005), 1, https://doi.org/10.1016/j.fluiddyn.2005.03.002.
[18] N. A. Hill, T. J. Pedley, and J. O. Kessler, *Growth of bioconvection patterns in a suspension of gyrotactic micro-organisms in a layer of finite depth*, J. Fluid Mech., 208 (1989), pp. 509–543, https://doi.org/10.1017/S0022112089002922.
[19] JuliaCollections and contributors, *Datastructures.jl*, 2023, https://github.com/JuliaCollections/DataStructures.jl (accessed 2025-8-25). Version v0.18.22.
[20] J. O. Kessler, *Hydrodynamic focusing of motile algal cells*, Nature, 313 (1985), pp. 218–220, https://doi.org/10.1038/313218a0.
[21] S. U. Khan, K. Al-Khaled, A. Aldabesh, M. Awais, and I. Tlili, *Bioconvection flow in accelerated couple stress nanoparticles with activation energy: bio-fuel applications*, Sci. Rep., 11 (2021), 3331, https://doi.org/10.1038/s41598-021-82209-0.
[22] D. R. Kincaid and E. W. Cheney, *Numerical Analysis: Mathematics of Scientific Computing*, vol. 2, American Mathematical Soc., 2009.
[23] S. Kitsunezaki, R. Komori, and T. Harumoto, *Bioconvection and front formation of Paramecium tetraurelia*, Phys. Rev. E, 76 (2007), 046301, https://doi.org/10.1103/PhysRevE.76.046301.
[24] H. G. Lee and J. Kim, *Numerical investigation of falling bacterial plumes caused by bioconvection in a three-dimensional chamber*, Eur. J. Mech. B Fluids, 52 (2015), pp. 120–130, https://doi.org/10.1016/j.euromechflu.2015.03.002.
[25] J. B. Loefer and J. Mefferd, R. B., *Concerning pattern formation by free-swimming microorganisms*, Am. Nat., 86 (1952), pp. 325–329, https://doi.org/10.1086/281740.
[26] E. N. Lorenz, *Deterministic Nonperiodic Flow*, J. Atmos. Sci., 20 (1963), pp. 130–141, https://doi.org/10.1175/1520-0469(1963)020⟨0130:DNF⟩2.0.CO;2.
[27] J. Manyer, A. F. Martín, and S. Badia, *Gridapsolvers.jl: Scalable multiphysics finite element solvers in Julia*, J. Open Source Softw, 9 (2024), 7162, https://doi.org/10.21105/joss.07162.
[28] A. M. Mil-Martínez, R. O. Vargas, A. Gómez-López, A. Zacarías, J. P. Escandón, E. García-Leal, and R. Mil-Martínez, *Numerical Simulation of Gravitactic Bioconvection with Nanoparticles: An Application of Solids Removal in Wastewater Using a Thermal Source*, Micromachines, 16 (2025), 553, https://doi.org/10.3390/mi16050553.
[29] J. D. Murray, *Mathematical Biology: I. An Introduction*, vol. 17, Springer Science & Business Media, 2007.
[30] T. J. Pedley, N. A. Hill, and J. O. Kessler, *The growth of bioconvection patterns in a uniform suspension of gyrotactic micro-organisms*, J. Fluid Mech., 195 (1988), pp. 223–237, https://doi.org/10.1017/S0022112088002393.
[31] T. J. Pedley and J. O. Kessler, *Hydrodynamic Phenomena in Suspensions of Swimming Microorganisms*, Annu. Rev. Fluid Mech., 24 (1992), pp. 313–358, https://doi.org/10.1146/annurev.fl.24.010192.001525.
[32] J. R. Platt, *"Bioconvection patterns" in Cultures of Free-Swimming Organisms*, Science, 133 (1961), pp. 1766–1767, https://doi.org/10.1126/science.133.3466.1766.

[33] M. S. Plesset and H. Winet, *Bioconvection patterns in swimming microorganism cultures as an example of Rayleigh–Taylor instability*, Nature, 248 (1974), pp. 441–443, https://doi.org/10.1038/248441a0.

[34] L. Rayleigh, *On convection currents in a horizontal layer of fluid, when the higher temperature is on the under side*, Philos. Mag. (6), 32 (1916), pp. 529–546, https://doi.org/10.1080/14786441608635602.

[35] W. J. Robbins, *Patterns Formed by Botile Euglena gracilis var. bacillaris*, Bull. Torrey Bot. Club, 79 (1952), pp. 107–109, https://doi.org/10.2307/2481929.

[36] L. Rothschild, *Measurement of Sperm Activity before Artificial Insemination*, Nature, 163 (1949), pp. 358–359, https://doi.org/10.1038/163358a0.

[37] P. Sagadevan, U. Raju, M. Murugesan, U. Fernandez-Gamiz, and S. Noeiaghdam, *Chemical reactions with the Casson nanofluid flow by the bioconvective behavior of microorganisms over a spinning disc*, Heliyon, 11 (2025), e41238, https://doi.org/10.1016/j.heliyon.2024.e41238.

[38] B. L. Taylor, *How do bacteria find the optimal concentration of oxygen?*, Trends Biochem. Sci., 8 (1983), pp. 438–441, https://doi.org/10.1016/0968-0004(83)90030-0.

[39] F. Verdugo and S. Badia, *The software design of Gridap: A Finite Element package based on the Julia JIT compiler*, Comput. Phys. Commun., 276 (2022), 108341, https://doi.org/10.1016/j.cpc.2022.108341.

[40] G. H. Wadhams and J. P. Armitage, *Making sense of it all: bacterial chemotaxis*, Nat. Rev. Mol. Cell Biol., 5 (2004), pp. 1024–1037, https://doi.org/10.1038/nrm1524.

[41] O. C. Zienkiewicz and R. L. Taylor, *The Finite Element Method Set*, Elsevier, 2005.